PCCP

Dopant driven tuning of hydrogen oxidation mechanism at the pore/nickel/zirconia triple phase boundary

Journal:	*Physical Chemistry Chemical Physics*
Manuscript ID	CP-ART-12-2017-008572.R1
Article Type:	Paper
Date Submitted by the Author:	07-Mar-2018
Complete List of Authors:	Iskandarov, Albert; Tokyo Institute of Technology, Materials Research Center for Element Strategy Tada, Tomofumi; Tokyo Institute of Technology, Materials Research Center for Element Strategy

Journal Name

ARTICLE TYPE

Cite this: DOI: 10.1039/xxxxxxxxxx

Dopant driven tuning of hydrogen oxidation mechanism at the pore/nickel/zirconia triple phase boundary†

Albert M. Iskandarov[a,b,c] and Tomofumi Tada,[a,b]

Received Date
Accepted Date

DOI: 10.1039/xxxxxxxxxx

www.rsc.org/journalname

The effects of cation dopants in zirconia on the H_2 oxidation mechanism at the pore/nickel/zirconia triple phase boundary (TPB) were theoretically examined. Y, Sc, Al, Ce, and Ca were considered as dopants, and on-boundary, O-migration, and H-migration reaction mechanisms were examined. Based on density functional theory calculations, Y as a dopant favored the on-boundary mechanism with water molecule formation within the immediate proximity of the TPB. The corresponding rate-limiting step is H transfer from the nickel surface to the boundary. In contrast, the on-boundary mechanism is not completed with the Al-, Sc-, and Ca-doped systems, due to the dissociation of water molecules at the boundary. In the Al-doped system, the O-migration mechanism is the major reaction pathway due to a low barrier for the rate-limiting step that corresponds to O transfer from zirconia to the nickel surface. H-migration mechanism, which implies water molecule formation on the zirconia surface at a position distant from the boundary, should dominate at the Sc-, Ca, and Ce-doped TPBs, with the lowest activation barrier at the Sc-doped TPB. The reasons for the switching of the reaction mechanisms depending on dopant species are analyzed.

1 Introduction

Fuel oxidation lies at the very heart of solid oxide fuel cell (SOFC) operation. Thus, it is considered that one of the main approaches to improve SOFC performance is closely related to understanding the reaction mechanisms. In conventional SOFCs, the oxidation reactions proceed at the triple phase boundaries (TPBs) where the electrolyte material, metal, and gas molecules meet. The electrolyte material enables ion transport to the TPB from the electrolyte connected to the anode/cathode, while pore allows gas molecules to access at the TPB, and the metal matrix, which is connected to a current collector, enables electronic current flow. The typical choice for the anode material in SOFCs is a nickel/yttria-stabilized zirconia (Ni/YSZ) cermet. Wide utilization of this anode compound has motivated intensive effort and discussion aimed at revealing the reaction mechanisms with this material, from both theoretical[1–10] and experimental[11,12] perspectives.

Experimental techniques cannot reveal the details of fuel oxidation at the atomic level; therefore, various atomistic modeling techniques have been widely used to study the mechanisms of the fuel oxidation reactions. In particular, theoretical calculations based on density functional theory (DFT) can provide reliable information on each step of such a complicated reaction as fuel oxidation. Moreover, modern simulation packages based on the DFT approach can handle systems that consist of various atomic species and contain hundreds of atoms, which has allowed rather complicated TPB structures to be considered. In the last decade, there have been several extensive DFT-based modeling studies that aimed to determine the most favorable mechanism for fuel oxidation at Ni/YSZ TPBs. In their first work on hydrogen oxidation in a Ni/YSZ system, Shishkin et al. suggested that the reaction was plausible in the considered Ni/YSZ system with an oxygen-rich TPB region, while very high energy barriers were reported for a stoichiometric TPB composition[1]. Let us make a critical remark here regarding the definition of the term *spillover* to avoid the confusion related to definition of reaction mechanisms[7]. The *spillover* term implies water molecule formation on the nickel or zirconia surface at a large distance from the TPB where no effect of the TPB on water molecule formation can be expected. Although the *spillover* term is widely used in DFT studies of fuel oxidation in Ni/YSZ systems, small sizes of the considered models do not allow to exclude completely such effect of the TPB. Thus, instead of the *spillover* term, we use the *migration* term to define the reaction mechanisms in the present

[a] *Materials Research Center for Element Strategy, Tokyo Institute of Technology, 4259-SE-3 Nagatsuta-cho, Midori-ku, Yokohama, Japan. Email: tada.t.ae@m.titech.ac.jp*
[b] *CREST, Japan Science and Technology Agency, K's Gobancho, 7, Chiyoda-ku, Tokyo 102-0076, Japan*
[c] *Institute for Metals Superplasticity Problems of the Russian Academy of Sciences, Khalturin St. 39, Ufa 450001, Russia*

† Electronic Supplementary Information (ESI) available: Energy barriers for the examined reaction mechanisms at 1000 K. See DOI: 10.1039/b000000x/

paper as follows: H-migration indicates transfer of a hydrogen atom from the nickel surface to an oxygen ion (on the zirconia surface) situated far from the TPB, O-migration indicates transfer of an oxygen ion from the zirconia surface to the nickel surface, OH^--migration indicates transfer of a hydrogen atom from nickel to the YSZ surface to form a hydroxyl that further migrates back to the nickel surface and forms a water molecule there with another hydrogen atom. Shishkin *et al.* distinguished another reaction mechanism that involves successive transfers of two H atoms from the nickel surface to an oxygen ion bonded to both nickel and zirconium atoms.[3] We refer to this mechanism as to the on-boundary mechanism throughout the rest of the present paper. According to this mechanism, a water molecule is formed in the vicinity of the TPB and thus does not require H migration along the YSZ surface, which is involved in H-migration mechanism when a water molecule is formed on the zirconia surface at some distance from the TPB.

The barriers for the on-boundary mechanism were reported by Shishkin *et al.* to be the smallest in comparison with those of the H-, O- and OH^--migration mechanisms[3]. The on-boundary mechanism was also predicted by Cucinotta *et al.* to be more favorable under dry conditions than the O- and OH^--migration mechanisms[4]. This result is also qualitatively consistent with the DFT analysis performed by Liu *et al.*, where the O-migration and on-boundary mechanisms were considered at different TPB sites[7]. In contrast to these DFT results, Fu *et al.* reported that that the energy barrier for the O-migration mechanism can be comparable with that for the on-boundary mechanism, which indicates the possibility of two concurrent reaction mechanisms. Moreover, even for qualitatively the same conclusion of on-boundary mechanism dominance, the energy barriers estimated by the different authors were notably different. These discrepancies can be attributed to differences in local atomic arrangements near the TPBs, the model sizes, and the dopant distributions. There is also a qualitative ambiguity of results based on micro kinetic modeling studies. Ammal *et al.* performed DFT-based micro kinetic modeling and concluded that the on-boundary mechanism dominates over H- and OH^--migration mechanisms[5]. However, Vogler *et al.*[2] reported that only under assumption of H-migration dominance was it possible to reproduce the experimental data derived by Bieberle *et al.*[11] for a patterned anode.

The dependence of reaction profiles on dopants is also an important aspect for SOFC design, although a many of the theoretical studies have focused only on Ni/YSZ. Recently, Liu *et al.* demonstrated that the energy barriers and reaction energies for H transfer from the Ni surface to interfacial oxygen ions can differ by 0.19 eV and 0.37 eV, respectively, depending on the types of cations near the oxygen ions[7]. Fu *et al.* demonstrated that if Ni atoms migrate into YSZ, then the barrier for O transfer from the zirconia to nickel surface can be as small as 0.88 eV, while the barrier is 1.36 eV when there are no Ni atoms in YSZ[13]. These theoretical results indicate that the reaction barriers can be changed according to the dopants involved, and in turn the reaction mechanism can be switched. However, the dopants used in SOFC anode materials have been mainly discussed only in terms of their effect on the oxygen-ion conductivity[14–16] and the stabilization of cubic phase zirconia at SOFC operating temperatures[17]. It has been well established that an 8 mol % concentration of yttria provides the maximum oxygen-ion conductivity[14,18]. There have also been theoretical studies on the optimal distribution of the yttrium dopant to improve the oxygen-ion conductivity[19–21]. However, dopants may also affect other properties in Ni/ZrO_2 systems. Muńoz *et al.* reported a pronounced effect for the Y dopant on the structure and adhesion of Ni/ZrO_2 interfaces[22]. Xu *et al.* also reported higher energy barriers for nickel atom migration on an Al-doped $(111)ZrO_2$ surface compared with that on the Y-doped surface[23]. Iskandarov *et al.* found that a dopant with a smaller covalent radius resulted in increased energy barriers for nickel diffusion at the $Ni(111)/ZrO_2(111)$ interface[24].

The literature data presented here implies that the properties of Ni/ZrO_2 systems can be modified by the cation dopants in a controlled manner. However, to the best of our knowledge, there has been no attempt to date, to theoretically predict the effect of cation dopants on the fuel oxidation mechanisms in SOFCs. From an atomistic modeling perspective, the task of studying fuel oxidation mechanisms becomes complicated due to the sensitivity of results (i.e., reaction energies and barriers) to such parameters as the examined structures with respect to geometry, composition, and dopants species. Thus, it is often difficult to justify appropriateness of the examined structures and the validity of results for comment on the actual electrochemical equilibrium in the anode of an SOFC.

Here we address the question of the cation dopant effect on the three main reaction mechanisms: on-boundary, H-migration, and O-migration mechanisms. We do not consider the OH^--migration mechanism, because it has not been reported as a dominant reaction pathway in any of the DFT-based literature. We examined effect of the divalent (Ca) and trivalent (Al, Sc, Y, Ce) dopants because these dopants are the most commonly used ones for zirconia[25–31]. Due to the lower valence compared with zirconium, these dopants lead to the formation of the oxygen vacancies in zirconia, which results in a high oxygen ion conductivity. The other known benefits that can arise from these dopants are stabilization of zirconia in the cubic phase[17], suppression of the nickel sintering in the SOFC anode[29,32], and enhanced coking resistance for hydrocarbon fuels[33]. The DFT calculations presented in this work are based on TPB models constructed in a systematic way to avoid dependence of reaction energies on model size[34]. We also apply open-circuit voltage (OCV) correction to the calculated reaction profiles to achieve an appropriate relation of the results to the electrochemical equilibrium in the SOFC anode.

2 Modeling setup

2.1 Structures

All structures used in this work are based on a model containing nickel and zirconia slabs, as shown in Fig. 1; the pure zirconia slab in the simulation cell contains 72 atoms and the Ni slab contains 36 atoms. This model has two characteristics: 1) the slab model for the metal is required to keep the bulk-like density of states (DOS) of the metal, and 2) the dependence of the reaction energy on the model shape and size should be minimized[34]. Besides, a

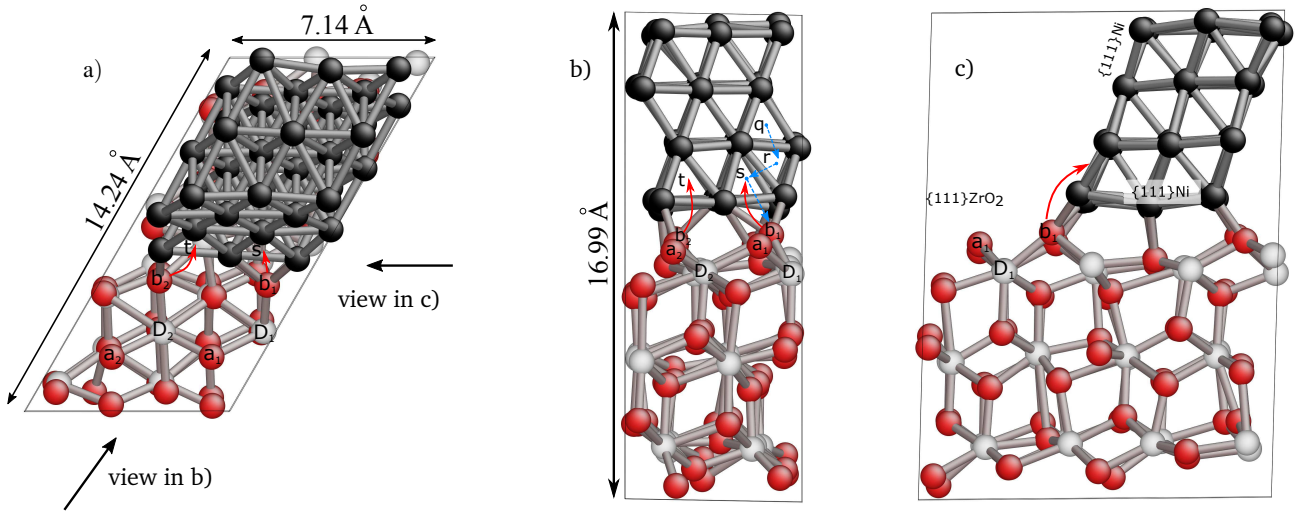

Fig. 1 a) Top view and b,c) side views of the relaxed Ni(111)/ZrO_2(111) interface. White, red and black spheres represent zirconium, oxygen, and nickel atoms, respectively. Some zirconia atoms located on the same $[\bar{1}10]$ line are labelled with the same character and numbered by subscript index. Blue arrows indicate jumps of hydrogen atoms on the nickel surface towards TPB in the course of the on-boundary and H-migration mechanisms. Red arrows indicate possible jumps of two oxygen ions, b_1 and b_2, from the TPB to the nickel surface during the O-migration mechanism.

line-shaped boundary between Ni and ZrO_2 was adopted because the boundary was found to be more electrochemically active than a point-contact boundary in terms of the chemical softness[35]. Periodic boundary conditions are imposed in all three dimensions. The geometry of the structure is selected so that the nickel slab is formed by the most stable surfaces, i.e., {111}[36]. Two {111} nickel surfaces form two interfaces with a zirconia slab, while the other two {111} nickel surfaces are exposed to the vacuum region (see Fig. 1c). The orientation and termination of the zirconia slab surface are chosen to be O-terminated {111} because this has the lowest energy among the other low-index zirconia surfaces under anodic conditions[34,37–39]. The location of the dopants and oxygen vacancies is determined by a search of their most stable configurations, the results of which are summarized in a later section. For all dopant species, we prepared reactant structures with the same arrangements of atoms at the TPB, as shown in Fig. 1, that is, oxygen ion at the b_1 site is bonded with two Ni atoms and a dopant at the D_1 site, and oxygen ion at the b_2 site is bonded with one Ni atom and a dopant at the D_2 site.

It should be noted that when zirconia is doped with some of the considered dopant species, other phases can appear, for example $CaZrO_3$[40] and Al_2O_3[29]. Presence of these phases in anode can significantly affect SOFC performance[29,41]. Therefore, ideally, the possibility of formation of these phases should be considered in simulations of SOFC anodes. However, experimental characterization of TPB structures on atomic level is still a big challenge; therefore, there have been no direct observations of atomic structure and composition of TPBs in actual SOFCs. Also, there have been no atomistic simulations that could suggest realistic structure of TPBs containing such phases as $CaZrO_3$ or Al_2O_3. As a result, including these phases in our simulations would cause additional uncertainties related to building realistic TPB structure for each particular phase. Therefore, in this work we did not consider the possibility of formation of these phases and simply assumed that few dopant atoms can appear at the TPB of Ni/ZrO_2.

2.2 Computational details

DFT calculations were performed using the Vienna Ab initio Simulation Package (VASP)[42,43] by electronic structure calculations based on the projector-augmented wave (PAW) method[44] and the generalized gradient approximation (GGA) according to Perdew, Burke and Ernzerhof (PBE)[45]. Spin-polarized calculations were employed with the kinetic energy of the plane waves being limited by 400 eV. The Brillouin zone was sampled with a $2 \times 1 \times 1$ k-point mesh. The choice of the cut-off energy and the k-point mesh is based on the convergence analysis performed by Xia[46] and previous works on Ni/ZrO_2 systems[1,7,38]. Atomic relaxations were stopped when components of the forces acting on atoms were less than 0.04 eV/Å. The shape and size of the simulation cell were kept fixed during relaxations. The convergence parameter for electronic relaxation was 10^{-5} eV. The 12 ($4s^2 4p^6 5s^1 4d^3$) electrons of Zr atoms, 6 ($2s^2 2p^4$) electrons of O atoms, and 10 ($3d^9 4s^1$) electrons of Ni atoms were treated as valence electrons. For Ce atoms, the 12 ($5s^2 5p^6 4f^1 5d^1 6s^2$) electrons were treated as valence electrons. For Ce, DFT+U methodology was utilized according to Dudarev *et al.*[47] to account for the localization of strongly correlated electrons[48]. The Hubbard parameter U was set to 5 eV for the Ce 4f orbitals[15,16]. For the Sc and Y atoms, 11 electrons were treated as valence electrons, $3s^2 3p^6 3d^2 4s^1$ and $4s^2 4p^6 4d^2 5s^1$, respectively. The $3s^2 3p^1$ electrons were treated as valence electrons for Al. For Ca, 10 electrons were treated as valence electrons, i.e., $3s^2 3p^6 4s^2$. To determine the transition states between reaction states and estimate the corresponding energy barriers, climbing nudge elastic band (NEB) calculations were performed, as implemented in VASP by Henkelman *et al.*[49].

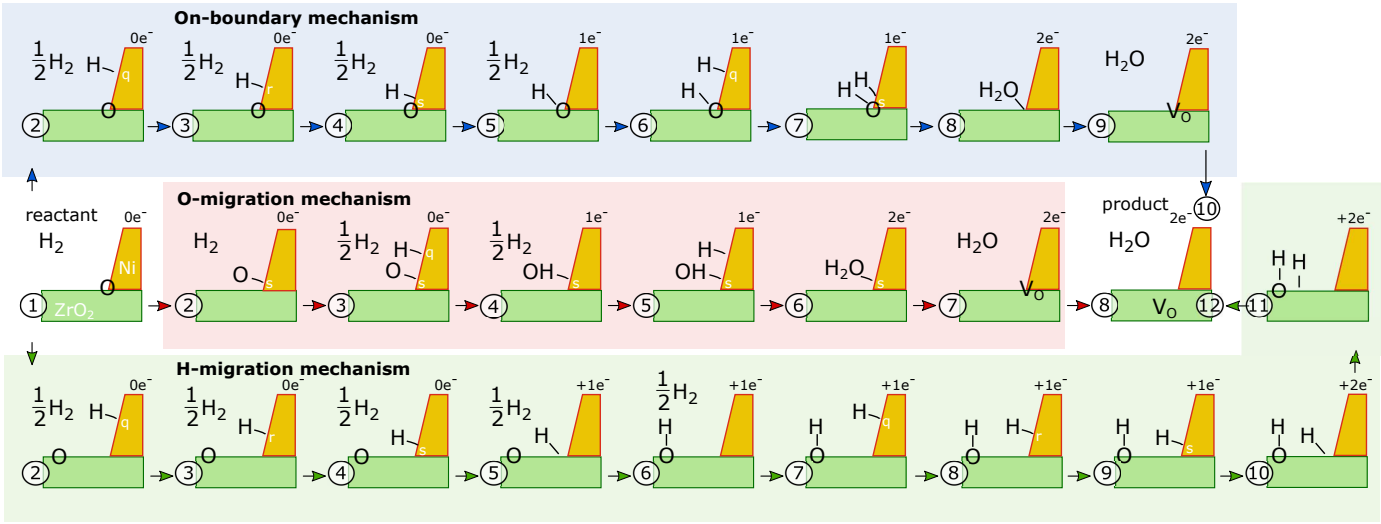

Fig. 2 Schematic illustration of the studied reaction pathways. Blue, red, and green areas span intermediate states of the on-boundary, O-migration, and H-migration mechanisms, respectively. Encircled numbers indicate sequence numbers for the reaction states along corresponding pathways. The number of electrons (transferred to nickel) used for the OCV correction is specified above each state. For each mechanism, only the oxygen ion that forms the water molecule is depicted.

2.3 Reaction mechanisms

Three reaction mechanisms of H_2 oxidation are considered, all of which are based on the following assumptions:

- All reactions start from an oxygen-rich structure (reactant configurations), which is attained by introducing an extra oxygen ion into X-doped zirconia slabs, where X indicates a divalent/trivalent dopant. This assumption is based on the use of a stoichiometric X-doped zirconia slab as a reactant configuration, whereby the reaction energies for the fuel oxidation reaction become highly endothermic. Thus, the reaction will not proceed from a stoichiometric system, and an oxygen-rich situation will consequently appear as a result of the supply of oxygen ions from the bulk solid electrolyte.

- All reactions end with stoichiometric structures (product configurations) because an oxygen ion in the reactant structure is used to form the gaseous water molecule.

- Gaseous H_2 molecules can be easily dissociated into atomic hydrogen on the nickel surface, and atomic H migrates easily on the Ni surface[50,51]. According to DFT calculations, the dissociation barrier of H_2 on the (111) nickel surface can reach only up to 0.25 eV[51], and the maximum barrier for H atom migration on the (111) nickel surface was estimated in the present work to be 0.3 eV. These energy barriers are small and those steps are thus omitted in the determination of the rate-limiting steps.

- An OCV correction[52] is adopted to maintain the electrochemical equilibrium in each Ni/X-doped zirconia anode.

- Effect of temperature is estimated by adding entropic contributions of gaseous molecules and is discussed in Section4.1.

Intermediate states of the three mechanisms are schematically illustrated in Fig. 2. The first mechanism, the on-boundary reaction, implies consecutive transfer of two hydrogen atoms from the nickel surface to zirconia, which leads to the water molecule formation with an oxygen ion at the immediate proximity of the TPB. In the course of the second mechanism, O-migration, the oxygen ion located at the TPB migrates to the nickel surface and combines there with two hydrogen atoms to form a water molecule. The third mechanism, H-migration, is qualitatively similar to the first mechanism, except that water formation occurs on the zirconia surface at some position distant from the TPB. This requires additional steps of hydrogen-atom migration along the zirconia surface.

It should be noted that the reaction energy profile for the H-migration mechanism is built from the results obtained for the on-boundary mechanism. States 1-5 are identical for both mechanisms. The energy of state 6 in the H-migration mechanism was estimated based on the structure, in which the hydrogen atom is bonded to the oxygen ion at site a_1 (see Fig. 1). This configuration aims to mimic the position of the hydroxyl at some distance from the TPB. We further assume that the transferred hydrogen atom bonded to O at the a_1 site does not contribute to the energy barrier for migration of the second hydrogen atom along the nickel surface and its transfer to zirconia. Thus, states 7-11 of the H-migration mechanism are qualitatively identical to states 2-6; therefore, it is assumed that the energy barriers related to the second hydrogen transfer and migration (states 7-11) are equal to those of the first hydrogen atom (states 2-6).

In our DFT calculations, the gaseous molecules depicted in Fig. 2 were not explicitly included into the simulation cell, but their energies were accounted for in the energy profiles. The total energies of the gaseous molecules were individually estimated in separate VASP calculations.

2.4 Open-circuit voltage (OCV) correction

In this section, we introduce the OCV correction to regard the oxygen-rich models as relevant reactants in the fuel oxidation re-

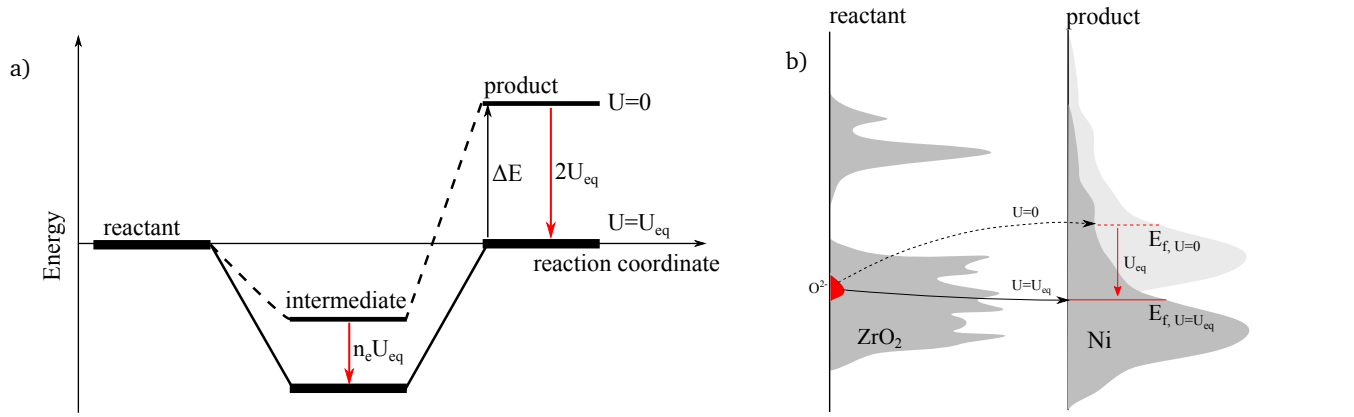

Fig. 3 a) Schematics for OCV correction of the reaction energy profile derived from DFT calculations (dashed line). b) Schematic illustration for DOS of ZrO_2 (left) and Ni (right).

actions. When the total system of a fuel cell is in equilibrium, we can assume local equilibrium in both the cathode and anode (i.e., an OCV situation). Under the OCV condition, the rates of the forward and backward electrochemical reactions in the anode (and also in the cathode) should be the same to maintain zero current. From an energetic point of view, this situation corresponds to zero reaction free energy. To attain zero reaction free energy, we make use of an energy correction term U that is applied for each electron transferred to nickel. This term is used to correct free energy of a reaction state by $-n_eU$, where n_e is the number of electrons transferred to nickel in the reaction state (as shown in Fig. 2). In total, two electrons are transferred to nickel in the course of HOR. Therefore, zero reaction free energy can be obtained after correction with $U = U_{eq} = \Delta E/2$, where ΔE is reaction free energy before correction. Figure 3a schematically shows the change of the reaction energy profile due to the OCV correction.

To clearly explain background for the OCV correction, let us first present the original approach proposed by Nørskov *et al.*[52] for the following water formation reaction at the cathode of a proton conductor fuel cell:

$$\frac{1}{2}O_{2(g)} + 2\left(H^+_{(electrolyte)} + e^-_{(Pt:C)}\right) \rightarrow H_2O_{(g)}, \quad (1)$$

where O_2 and H_2O molecules are in the gas phase, H^+ is a proton coming from the electrolyte, and $e^-_{(Pt:C)}$ represents an electron at the cathode. The calculation for the total energy of the left hand side of Equation (1) could be very easy if the molecular energy of $\frac{1}{2}H_{2(g)}$ is available. To do so, an anodic equilibrium (i.e., $\frac{1}{2}H_{2(g)} = H^+_{(electrolyte)} + e^-_{(Pt:A)}$) can be introduced, where $e^-_{(Pt:A)}$ represents an electron at the anode. Using this relation, the cathodic reaction of Equation (1) can be written as:

$$\frac{1}{2}O_{2(g)} + H_{2(g)} + 2\left(e^-_{(Pt:C)} - e^-_{(Pt:A)}\right) \rightarrow H_2O_{(g)}, \quad (2)$$

To maintain the local equilibrium at the cathode, the free energies of the left- and right-hand sides have to be equal, and this is simply realized with the electrode potential term $2(e^-_{(Pt:C)} - e^-_{(Pt:A)})$ because the term can be used to compensate the free energy difference between $\frac{1}{2}O_{2(g)} + H_{2(g)}$ and $H_2O_{(g)}$. That is, the estimated potential energy difference between the cathode and anode under the OCV condition corresponds to the free energy difference between $\frac{1}{2}O_{2(g)} + H_{2(g)}$ and $H_2O_{(g)}$. In this way, any configuration can be calculated with DFT as a neutral system, and we simply add the correction term to the system free energy according to the number of transferred electrons in each reaction step. Let us write the correction energy as U, which is equal to half of the free energy difference between $\frac{1}{2}O_{2(g)} + H_{2(g)}$ and $H_2O_{(g)}$, because the number of transferred electrons in Equation (2) is two. As a general expression, the energy of a reaction state with n_e electrons on Pt is shifted by $-n_eU$.

Now let us adopt the idea of the OCV correction for the following hydrogen oxidation reaction (HOR) in the nickel/zirconia anode of an SOFC:

$$H_{2(g)} + O^{2-}_{(ZrO_2)} \rightarrow H_2O_{(g)} + 2e^-_{(Ni)}, \quad (3)$$

where $O^{2-}_{(ZrO_2)}$ is the extra oxygen ion in the doped-zirconia slab. To achieve the OCV correction in Equation (3), we again equalize the free energies of the left- and right-hand sides. To make the point clearer, let us rewrite the equation as:

$$H_{2(g)} + O_{(ZrO_2)} + 2e^-_{(X)} \rightarrow H_2O_{(g)} + 2e^-_{(Ni)}, \quad (4)$$

where $2e^-_{(X)}$ is the extra electron at material X (i.e., ZrO_2 or Ni), and O_{ZrO_2} is the extra neutral oxygen in the doped-zirconia slab. If X is equal to Ni, then there is no chance to find the correction term U. However, the material that should be assigned to X is ambiguous, because Equation (4) is the total reaction of anode, and equilibrium must be realized for the reaction, i.e., X could be Ni and ZrO_2. Once X is assigned as ZrO_2, the situation for the excess electrons $2e^-_{(X)}$ could become very complicated because the electron can occupy states in the valence band, gap states, etc. (e.g., see Fig. 3b). As a consequence, Equation (4) can be written as:

$$H_{2(g)} + O_{(ZrO_2)} + 2\left(e^-_{(X)} - 2e^-_{(Ni)}\right) \rightarrow H_2O_{(g)}, \quad (5)$$

This expression is quite similar to that of Equation 2, and we thus recognize that the free energy difference between $H_{2(g)} + O_{(ZrO_2)}$ and $H_2O_{(g)}$ can be set to two times the value of U, the OCV correc-

Table 1 Energies (eV) of the oxygen-rich reactant structures with two trivalent dopants and no oxygen vacancies. The energies are relative to the structure with two dopants located at sites D_1 and D_2. NN designates the nearest-neighbor configuration between the dopants, and NNN designates the next-nearest-neighbor configuration between the dopants

Dopant	D_1-D_2 (NN)	D_1-D_3 (NN)	D_1-D_4 (NNN)	D_3-D_5 (NN)
Y	0.00	+0.21	+0.05	+0.26
Ce	0.00	+0.81	+0.84	+1.08
Sc	0.00	−0.21	−0.23	−0.19
Al	0.00	−0.89	+0.17	−0.57

tion term. In this way, we apply the OCV corrections to the HOR in the nickel/zirconia anode of the SOFC. Note that, in contrast to the OCV correction for the oxygen reduction reaction (ORR) in a proton conductor fuel cell, the U value in HOR is not based on the free energy difference between $\frac{1}{2}O_{2(g)}+H_{2(g)}$ and $H_2O_{(g)}$, because the oxygen is not a gas but an atom embedded in ZrO_2, which consequently results in a much smaller value of U for the HOR than that for the ORR.

As for the computation steps, we first build the reaction energy profile solely based on the total electronic energies calculated with DFT for the neutral systems along the HOR reaction, $H_{2(g)}+O_{(ZrO_2)}\rightarrow H_2O_{(g)}$. Second, entropic contribution of gaseous molecules is added for each state to obtain reaction energy profile based on the free energies. Third, the OCV correction is performed.

We have described how the OCV correction term U_{eq} can be individually determined for each dopant X from the DFT reaction energy ΔE at the X-doped TPB. This procedure to determine U_{eq} corresponds to the situation when dopant X is the major (or the only) dopant appearing at the TPB. This correction is referred to as the individual OCV correction. On the other hand, a different situation could occur when co-doping by X is performed in a conventional Ni/YSZ anode, i.e., X is a minor dopant and Y is the major dopant. The concentration of the co-dopant in YSZ is assumed to be significantly smaller than that of Y. In this situation, the equilibrium of HOR in anode is primarily determined by condition of HOR equilibrium at the Y-doped TPBs. Therefore, the DFT reaction energy profiles for the co-dopant should be corrected using the OCV correction term U_{eq} determined for the Y-doped TPB, which is referred to as the YSZ-based OCV correction. For example, let us assume that ΔE_X and ΔE_Y are reaction free energies before the OCV correction at the X- and Y-doped TPBs, respectively. Then, in the situation of co-doping by X, the energy correction term U is $\Delta E_Y/2$, not $\Delta E_X/2$. Therefore, the same value of $U=\Delta E_Y/2$ is used for all dopants in the situation of co-doping.

3 Results

3.1 Defect distribution

3.1.1 Reactant configurations

For calculation of the HOR energy profile, the dopant positions in doped-ZrO_2 is the first concern because when dopants are positioned closely to reaction sites (i.e., active sites or a boundary),

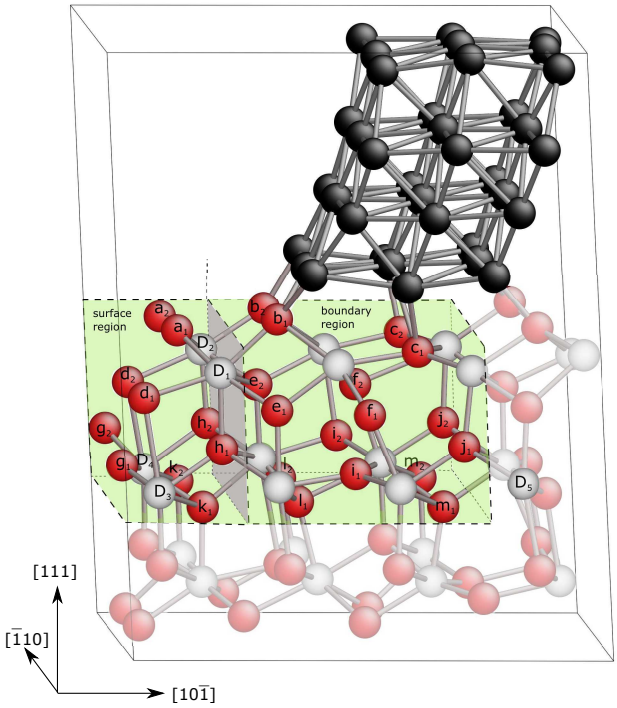

Fig. 4 TPB model used in the present paper. White, red and black spheres represent zirconium, oxygen, and nickel atoms, respectively. The green area indicates search region for the most energetically favorable position of the oxygen vacancy.

we can expect a significant influence of the dopants on the reaction energy profiles. For example, in Fig. 4, when dopants are positioned at cation site D_1, the dopant effect on the reaction energy profile at the Ni-ZrO_2 boundary will emerge directly. On the other hand, a dopant positioned at site D_3 will have less influence on interface reactions. To find possible positions for the dopants, the total energies were calculated as a function of the dopant positions.

In this study, the base structure of the oxide is cubic ZrO_2. The formal charges of Zr and O are +4 and −2, respectively, and the dopants adopted in this study are trivalent (+3) and divalent (+2) cations. We consider the following three cases:

Case i) when two Zr ions are replaced with two trivalent (+3) cations, a stoichiometric/one-oxygen-rich model contains one/zero oxygen vacancy,

Case ii) when a Zr ion is replaced with a divalent (+2) cation, a stoichiometric/one-oxygen-rich model contains one/zero oxygen vacancy, and

Case iii) when two Zr ions are replaced with two divalent (+2) cations, a stoichiometric/one-oxygen-rich model contains two/one oxygen vacancies. One-oxygen-rich configurations are used for determination of the dopant positions because these are the reactants of the HOR.

Let us start with Case i), with two trivalent dopants and no oxygen vacancy. Table 1 lists the total energies calculated for the doped configurations with respect to the doped structure with two dopants at sites D_1 and D_2. The most stable dopant configu-

Table 2 Energies (eV) of the oxygen-rich Ca-doped structures with one Ca dopant and no oxygen vacancies. The energies are relative to the structure with the dopant at site D_1

Dopant	D_1	D_2	D_3	D_5
Ca	0.00	−0.02	+0.64	+0.30

ration varies with the dopant species, i.e., D_1-D_2 for Y and Ce, D_1-D_4 for Sc, and D_1-D_3 for Al. For each dopant, the bulk dopant configuration (D_3-D_5) is not the most energetically favorable configuration. For all dopant species, the most stable configurations have a dopant at the D_1 position, near which all atomic and molecular movements are taking place in the course of the examined reaction pathways. Therefore, the local configuration around the D_1 site mainly affects the H_2 mechanism at the TPB, and the position of the second dopant has little influence on the reaction profiles as long as the first dopant is positioned at the D_1 site. For instance, for the Al-doped case we calculated energy barriers for the O-transfer step (1-2) of the O-migration mechanism with the D_1-D_n ($n=2-4$) dopant distributions, and found that the difference between the calculated barriers is 0.10 eV at the most. Therefore, even for the Al- and Sc-doped TPB, the D_1-D_2 dopant configuration provides useful results for understanding the dopant effect on the mechanisms of the H_2 oxidation. In addition, the fact that the configuration with a dopant at the position D_1 is the most stable configuration regardless of the dopant species indicates the possibility of a dopant segregation at the surface, which is actually reported in DFT studies on Y and Sc segregation at the (111) zirconia surface[24,38,53].

Let us proceed with Case ii), with a single divalent dopant and no oxygen vacancy. In Table 2 we present the total energies of the doped structures relative to the structure with the dopant located at the D_1 site. For Ca, the dopant prefers to be located at the position D_2, which indicates that for Ca there should also be a tendency of segregation at the surface and TPB. We would like to pay additional attention to the both bulk positions (D_3 and D_5) of the dopant, which are attributed with higher energies than both the surface positions (D_1 and D_2).

For Case iii), with two divalent dopants and one oxygen vacancy, we did not perform calculations to find the most stable configuration of the two dopants, but we assumed that they should be located at positions D_1 and D_2, as with Case ii), because Ca prefers these to positions D_3 and D_5.

The search performed for the dopant position was not rigorous because only five possible positions for the dopants were considered. However, we consider that for all dopants species, the results presented here provide sufficient justification for the consideration of atomistic models with dopants segregated at the TPB. Thus, in the present work, it was assumed that the TPB models contain two dopants located at sites D_1 and D_2 except for the next case. We additionally considered an Y-doped structure with two Y dopants located at the inner positions D_3 and D_5. The results obtained for this structure are marked as Y in bulk throughout the present paper. The cations at the TPB (i.e., sites D_1 and D_2) are Zr in this structure; therefore, the results obtained for this structure are regarded as reference data to discuss the effect of the dopants.

Table 3 Most stable position for the first/second oxygen vacancy in the surface region and entire search region of the TPB structure with trivalent/divalent dopants

Dopant	Surface region	Entire search region
Y	g_2	l_1
Y in bulk	h_1	h_1
Ce	k_1	f_2
Sc	g_2	l_1
Al	d_1	d_1
Ca	k_1	k_1

Table 4 Total energy change ΔE_{Omig}, due to the transfer of oxygen ions from zirconia to the nickel surface

Dopant	ΔE_{Omig} (b_1 to s), eV	ΔE_{Omig} (b_2 to t), eV
Y	+1.22	+1.24
Sc	+1.16	+1.57
Al	+0.73	+1.51

3.1.2 Product configurations

In the product configurations we assume the same positions of the two dopants as in the reactant configurations, i.e. D_1 and D_2 (D_3 and D_5 in the Y in bulk structure). Therefore, in Case i), two trivalent dopants and one oxygen vacancy; only the position of a single oxygen vacancy must be additionally determined. For Case iii), two divalent dopants and two oxygen vacancies, rigorous identification of the most stable configuration of the two vacancies is very time consuming; therefore, we restrict possible vacancy configurations by placing the first vacancy at the c_2 site, so that only the position for the second vacancy must be determined.

We examined 26 possible vacancy positions within the search region shown as green in Fig. 4. This area contains oxygen ions of four upper oxygen layers, except for the ions located near the TPB on the opposite (close to the right boundary of the simulation cell) surface of the nickel slab. There are two oxygen ions in the simulation cell along each $[\bar{1}10]$ line; therefore, it is convenient to label these 13 lines within the search region by characters a-m. Each oxygen ion in the search region can then be identified by the line name and additional index (1 or 2), as shown in Fig. 4.

The search region is divided into surface and boundary regions; the vertical gray plane in Fig. 4 separates the search region into the two regions. The most stable position of the vacancy is assumed to be in the surface region for the H-migration mechanism because this mechanism implies the formation of an oxygen vacancy at some distance from the TPB. For the other two HOR mechanisms, the limitation for the vacancy positions was not applied (i.e., the most stable position of the oxygen vacancy is within the entire search region). Table 3 lists the most stable positions of the oxygen vacancy in the surface region and in the entire search region according to the dopants species.

3.2 O-migration mechanism

In the TPB model, there are two oxygen ions that are located within the immediate proximity of the TPB and could potentially migrate to the nickel surface, i.e., ions at positions b_1 and b_2 (see Fig. 1). We can determine which of the two anions is more likely to migrate on the basis of the total energy change ΔE_{Omig}, due to their transfers. An oxygen ion at position b_1/b_2 is assumed to transfer to position s/t on the nickel surface (Fig. 1b). Table 4 lists the calculated values of ΔE_{Omig} for Y, Sc, and Al; ΔE_{Omig} values for the b_1 to s process are smaller than those for b_2 to t. Therefore, transfer of the oxygen from position b_1 should be more probable than that from b_2, and we consider it as the first step of the O-migration mechanism. Note that the magnitude of the OCV correction in this analysis does not affect the result, because the number of electrons transferred to nickel is the same before and after O transfer (see step 1-2 in Fig. 2).

A climbing (nudged elastic band) NEB analysis was performed for step 1-2, which is transfer of the oxygen ion from position b_1 to s. Figure 5 shows the calculated reaction energy profiles for the O-migration mechanism after individual OCV correction, and the reaction energies before OCV correction ΔE. The energy barriers for step 1-2 are within the range of 0.87-1.80 eV, depending on the dopant species at the TPB. The transition state has only slightly higher energy than that of state 2. The reaction proceeds with H atom migration along the nickel surface (from position q to s in Fig. 1), the formation of OH (state 4), the formation of a water molecule (state 6), and then desorption of the water molecule (state 7). The energy barriers for the H jumps on the nickel surface are shown to be small and amount to only 0.05-0.3 eV.

The reaction further proceeds with migration of the oxygen vacancy into the bulk region (step 7-8). This migration is accompanied with a decrease of the total energy for all dopants. The preference for the oxygen vacancy to be located in the bulk region with respect to the surface is consistent with the previous theoretical reports[53]. States 7 and 8 differ only by the position of the oxygen vacancy, so that they are connected with each other through several elementary jumps of the oxygen vacancy. Explicit calculation of the energy barriers for all these jumps is very time consuming, especially considering the variety of paths that the oxygen vacancy can follow. Therefore, we instead use the results obtained by Pornprasertsuk *et al.*[14] for YSZ to determine the possibility of oxygen diffusion as the rate limiting step for the O-migration mechanism. Pornprasertsuk *et al.* performed extensive analysis of the energy barriers for oxygen-ion migration in bulk YSZ according to the types of cations that surround the migrating oxygen ion. We adopt these barriers for the atomic environment of the vacancy at site b_1 (state 7); the barrier for an elementary jump of the vacancy to position f_2 should be 0.80 eV, which is energetically more feasible than jumps to the two other nearest-neighbor sites of e_1 and e_2 (0.88 eV). Further migration of the vacancy (to the position in state 8) occurs in the dopant-depleted subsurface region, which should be accompanied by energy barriers not larger than 0.71 eV.

According to the last two paragraphs, we conclude that the

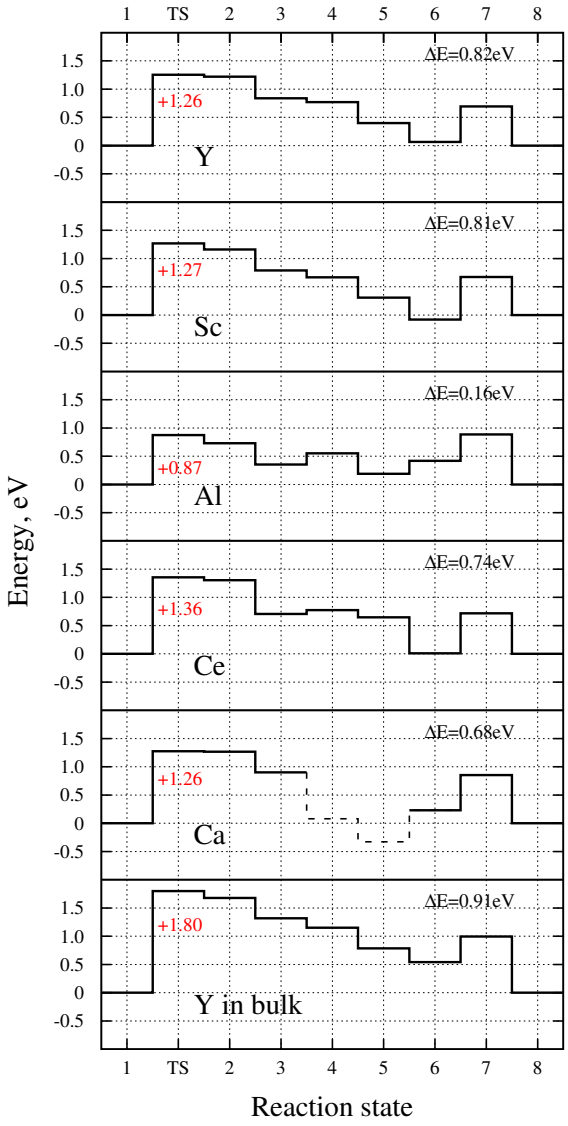

Fig. 5 Energy profiles for the HOR via the O-migration mechanism. Transition states are marked as TS.

rate-limiting step of O-migration mechanism for all dopants should be the transfer of the oxygen ion to the nickel surface (step 1-2). This result is in qualitative agreement with the literature data, where the same rate-limiting step for the O-migration mechanism was predicted in Ni/YSZ systems[1,4,13]. The energy barriers associated with the transition states of this rate-limiting step are listed in Table 5. However, it should be noted that OH migrates back to zirconia during atomic relaxation in states 4 and 5 in the Ca-doped system (the energies of these states after OH migration to zirconia are shown by the dashed line in Fig. 5). Thus, the HOR cannot be completed via O-migration in the Ca-doped system, even though the barrier of step 1-2 (+1.26 eV) is comparable with that for other dopants.

Let us next address the dopant effect. When dopants are located directly at the TPB (sites D_1 and D_2), the barrier of the rate-limiting step is within the range of 0.87-1.35 eV, which is no-

tably lower than 1.80 eV for the Y in bulk structure. Thus, dopant segregation at the TPB is beneficial for the O-migration mechanism. The lowest activation barrier (0.87 eV) for O-migration was obtained at the Al-doped TPB, and this barrier is at least 0.3 eV lower than that for all other dopants. This low energy barrier can indicate a high probability and high rate of the HOR via the O-migration mechanism at the Al-doped TPB. Thus, the origin of the low energy barrier at the Al-doped TPB must be revealed and is discussed further in a later section.

Previous discussion in this section is based on the individual OCV correction. The number of electrons in nickel for states 1 and 2 (see Fig. 2) is the same; therefore, the magnitude of the OCV correction does not affect the barrier height of the rate-limiting step 1-2. Therefore, this barrier for co-doping with each dopant should be same as that for the individual OCV correction. For co-doping, barriers for step 1-2 at Mg- and Sr-doped TPBs were additionally estimated to be 1.23 and 0.95 eV, respectively. However, at the Sr-doped TPB, similar to the Ca-doped TPB, the reaction cannot be completed via the O-migration mechanism due to the migration OH from the nickel surface to zirconia in states 4 and 5. Thus, only Al and Mg dopants allow the HOR to complete via O-migration with an activation barrier that is lower than that for Y. However, the activation barrier for Mg (1.23 eV) is almost equal to that for Y (1.26 eV); therefore, co-doping by Al (the barrier is 0.87 eV) could be expected to have a significant contribution to the HOR via the O-migration mechanism in the Ni/YSZ anode.

3.3 On-boundary mechanism

According to the analysis performed in the previous section, it should be energetically easier to remove an oxygen ion from a b_1 site than from a b_2 site. This also implies that it must be easier to detach a water molecule from the zirconia surface if the molecule is formed by an oxygen ion at position b_1 than at position b_2. Moreover, hydrogen atoms can directly jump from the s site to oxygen at b_1 over the bridge site between two nickel atoms (see Fig. 1). Thus, for the on-boundary and H-migration mechanisms, we consider the successive migration of two hydrogen atoms from position q via s towards the oxygen ion at the b_1 site. For the on-boundary mechanism, this first results in OH formation and then water-molecule formation with the oxygen ion at the b_1 site. A climbing NEB analysis was performed for several steps along this pathway: 2-3 (first jump of the first hydrogen atom along the Ni surface from position q to r), 3-4 (second jump of the first hydrogen atom along the Ni surface from position r to s), and 4-5/7-8 (transfer of the first/second hydrogen atom from position s on the nickel surface to the on-top position of oxygen at the b_1 site).

Figure 6 presents reaction energy profiles for the on-boundary mechanism after individual OCV correction. According to the NEB analysis, the migration of H along the nickel surface (steps 2-3 and 3-4) is associated with small energy barriers of around 0.05-0.30 eV, while the energy barriers for the H transfer steps to zirconia (step 4-5/7-8 for the first/second hydrogen transfer) are significantly higher (above 1.08/0.75 eV for step 4-5/7-8) for all dopants (see Table 5).

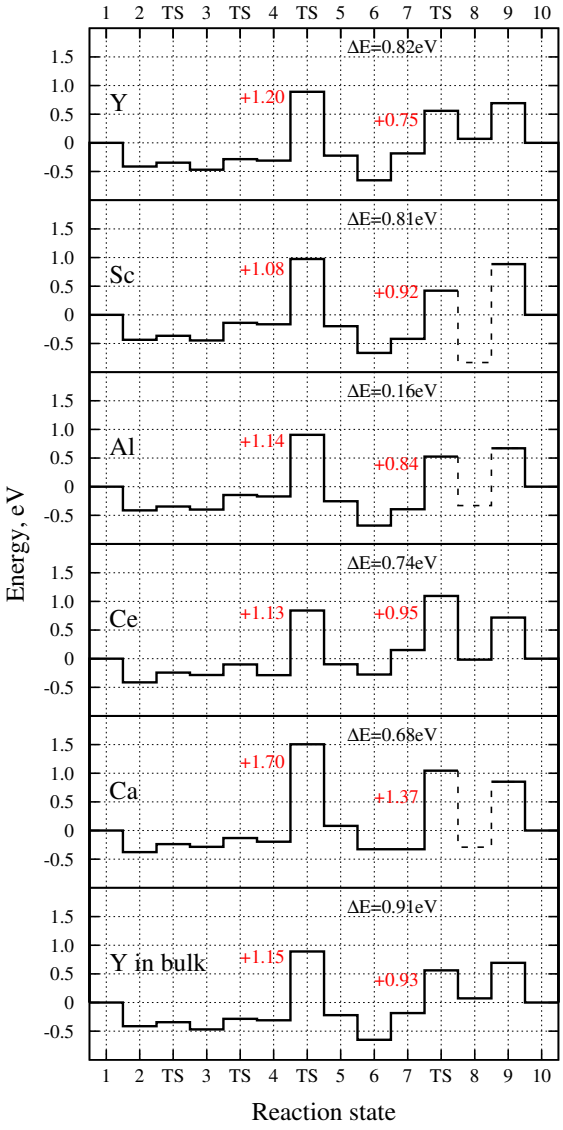

Fig. 6 Energy profiles for the HOR via the on-boundary mechanism. Transition states are marked as TS.

In state 8 of the Al-, Sc-, and Ca-doped structures, the water molecule is not stable and dissociates into a hydroxyl on top of the dopant at the D_1 site and a proton bonded with a surface oxygen (at a_1 or a_2 sites). For this reason, the energy of state 8 for Al, Sc, and Ca is marked by dashed lines in Fig. 6, which indicates that the HOR cannot be completed via the on-boundary mechanism for these three dopants. It should be noted that instead of the considered Langmuir-Hinshelwood-type step 7-8 that leads to the water molecule dissociation for Al, Sc, and Ca, one could propose Eley-Rideal-type step with direct interaction of OH adsorbed at some distance from the TPB with gaseous H_2. The Eley-Rideal-type step may possibly lead to successful formation of a gaseous water molecule at the Al-, Sc-, and Ca-doped TPB. As for the other dopants, a water molecule is adsorbed at the TPB in state 8, and corresponding adsorption energies for the Y in bulk, Y-, and Ce-doped structures are −0.56, −0.62, −0.74 eV, respectively. These

Table 5 Energy barriers (eV) for the three HOR mechanisms after different types of OCV correction

HOR mechanism	Reaction step	Type of OCV correction	Y	Sc	Al	Ce	Ca	Y in bulk
O-migration	1-2[a]	any	1.26	1.27	0.87	1.36	1.26[b]	1.80
On-boundary	4-5[a]	individual	1.20	1.08[c]	1.14[c]	1.13	1.70[c]	1.15
		YSZ-based	1.20	1.07[c]	0.97[c]	1.11	1.66[c]	1.18
		no	1.41	1.28[c]	1.18[c]	1.31	1.87[c]	1.38
	7-8	individual	0.75	0.92[c]	0.84[c]	0.95	1.37[c]	0.93
		no	0.95	1.12[c]	0.88[c]	1.13	1.54[c]	1.16
H-migration	4-5[a]	individual	1.20	1.02	1.14	1.07	1.70	1.15
	9-10[a]	individual	1.20	1.02	1.14	1.07	1.70	1.15

[a] The step is rate-limiting for the corresponding HOR mechanism.
[b] Migration of OH occurs from the nickel surface to zirconia, which does not allow the HOR to be completed via the O-migration mechanism.
[c] Dissociation of water molecule occurs at the TPB, which does not allow the HOR to be completed via the on-boundary mechanism.

values quantitatively agree with the adsorption energies of water molecules on YSZ surfaces reported by Shishkin *et al.*[54] as −0.52 eV and by Chaopradith *et al.*[55] as ranging from −1.19 to −0.5 eV.

Similar to the O-migration mechanism, the last step of the on-boundary mechanism (step 9-10) involves the migration of an oxygen vacancy from position b_1 to its position in the product configuration (state 10). The barriers for this oxygen diffusion, as estimated in the previous section, are lower than the barriers for step 4-5; therefore, oxygen diffusion should not be a rate limiting process of the on-boundary mechanism. We conclude that transfer of the first hydrogen (step 4-5) from the nickel surface to zirconia is the rate-limiting step for the on-boundary mechanism.

There is an electron transfer to nickel during the rate-limiting step 4-5 (see Fig. 2); therefore, the barrier for this step is dependent on the magnitude of the OCV correction. Thus, in the co-doping situation, the barrier of step 4-5 for each dopant is different from that after the individual OCV correction. The barriers for this step after the YSZ-based OCV correction are also listed in Table 5. The barriers for this step with co-doping by Mg and Sr were additionally estimated to be 1.29 and 1.54 eV, respectively. However, the HOR cannot be completed via the on-boundary mechanism in the case of Mg-doping due to dissociation of the water molecule at the TPB. Among the dopants for which the HOR can be completed via the on-boundary mechanism, Ce may be the most promising co-doping candidate because it has the lowest activation barrier.

3.4 H-migration mechanism

The first five states of the H-migration mechanism are identical to those of the on-boundary mechanism. However, compared with the on-boundary mechanism, the energies in the energy profile for the H-migration mechanism (Fig. 7) are different due to the different magnitudes of the OCV correction. The highest energy barrier among the first 5 steps corresponds to the hydrogen transfer from position s on the nickel surface to the oxygen ion at position b_1. States 5 and 6 differ only by position of the transferred H on the zirconia surface. The energy barriers required for H atom migration along the zirconia surface were not explicitly cal-

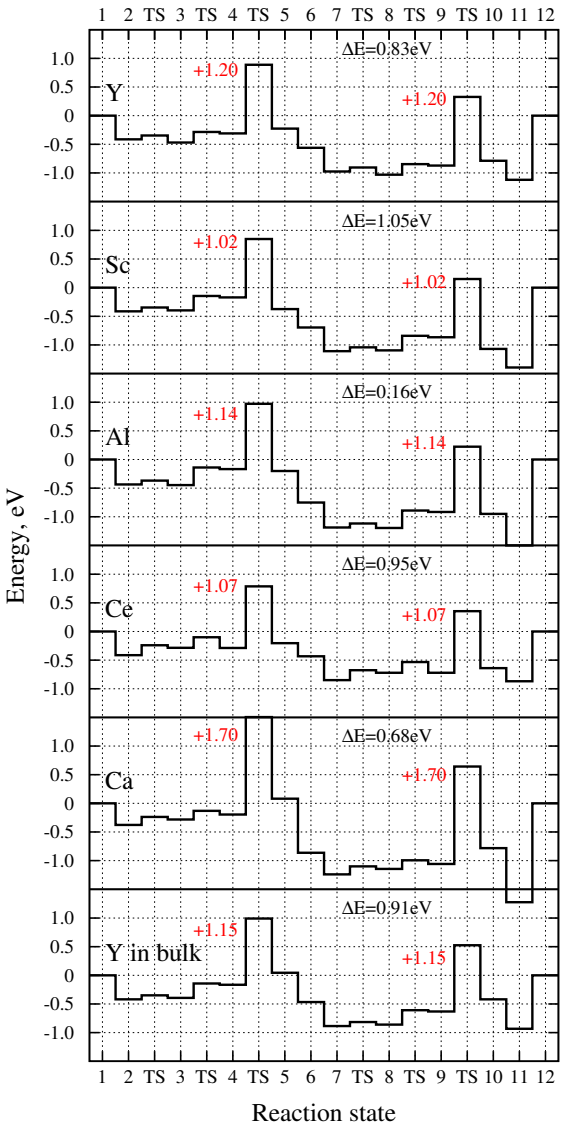

Fig. 7 Energy profiles for the HOR via the H-migration mechanism. Transition states are marked as TS.

culated, but instead the barriers estimated by Cucinota *et al.* for a Grotthus-like mechanism, i.e., H jumps on the YSZ surface among surface O ions, were adopted[4]. Such jumps of H require barriers of around 1 eV to be overcome.

States 7-11 are identical to states 2-6, and the corresponding energy barriers are the same. The last reaction step 11-12 can be represented as a sequence of three elementary events: i) H atom migration on the zirconia surface towards the first OH^-, which results in water molecule formation, ii) water molecule desorption from the zirconia surface, and iii) oxygen diffusion in zirconia, so that the surface oxygen vacancy formed after water desorption is filled with a bulk oxygen ion. The barrier for i) has been estimated in this section as 1 eV, that for ii) at the O-rich YSZ surface was estimated by Shishkin *et al.* to be 0.52 eV[54], and the barrier for iii) was estimated in the O-migration mechanism section to be not larger than 0.88 eV. Therefore, considering that the barriers for steps 4-5 and 9-10 are larger than 1 eV for all dopants, we conclude that the H transfer from the nickel surface to zirconia constitutes the rate-limiting step for the H-migration mechanism.

In the co-doping situation, the barrier of the rate-limiting steps 4-5 and 9-10 for H-migration is equal to that of step 4-5 of the on-boundary mechanism for every dopant. In contrast to the on-boundary mechanism, the H-migration mechanism can be successfully completed for all examined dopants. Sc exhibits the lowest activation energy (1.07 eV) among the dopant species that favor the H-migration mechanism in the co-doping case; therefore, Sc co-dopants would contribute to the most significant enhancement of the HOR via the H-migration mechanism.

4 Discussion

4.1 Dopant dependence of favorable HOR mechanism

We have considered three HOR mechanisms individually and clarified the influence of the dopants on the energy barriers for each mechanism. Here we compare the reaction mechanisms with respect to the dopants and specifically answer which mechanism is the most energetically favorable for each dopant species. For each dopant in Table 5, we should identify the reaction mechanism with the lowest activation energy (i.e., lowest energy barrier of the rate-limiting step). We begin the discussion in this section from the individual OCV correction. The co-doping situation is addressed in the last part of this section.

The activation energies for the on-boundary and H-migration mechanisms are the same at the Y-doped TPB (1.20 eV). These barriers are lower than the activation barrier of the O-migration mechanism (1.26 eV), which indicates that O-migration should not be the favored HOR mechanism at the Y-doped TPB. Next, we assume that when the activation energies for the on-boundary and H-migration mechanisms are same, the on-boundary mechanism should dominate. This assumption can be justified by consideration of the hydrogen transfer steps. If the activation energies are the same, then the energy barriers for the first hydrogen transfer step 4-5 are the same for both mechanisms. However, for each dopant, the barriers for the second hydrogen transfer in the on-boundary mechanism (step 7-8) are notably lower than those for the second hydrogen transfer in the H-migration mechanism (step 9-10), as shown in Table 5. Thus, the on-boundary mechanism should be dominant at the Y-doped TPB.

Various dominant HOR mechanisms were predicted in experimental works on Ni/YSZ anodes. Based experimental results and kinetic modeling, Ihara et al. predicted O-migration mechanism, where water formation on nickel surface occurred via reaction between adsorbed O and H species[56]. In contrast, Primdahl et al. proposed that the O-migration was unlikely, because H-migration mechanism should dominate due to dissociative adsorption and fast migration of hydrogen on the nickel surface[57]. Similar conclusion was made by Vogler et al.[2]. Nagasawa et al. proposed that the H- and O-migration mechanisms can undergo simultaneously[58,59]. Since our simulations focus only on the TPB reactions, we do not investigate other processes such as bulk and surface diffusion of oxide ions, which, in contrast, were considered in the kinetic models based on experimental data. Therefore, we cannot directly compare our results with those from the experimental studies. In our paper we assume that the bulk/surface oxide ion diffusion is not a rate-limiting process, and thus HOR steps can be regarded as the rate-limiting steps. Under this limited condition we can compare our results with the experimental ones. Activation energies of Ni/YSZ calculated in our work for all three reaction mechanisms are almost the same (1.20 eV for the on-boundary and H-spillover mechanisms, and 1.26 eV for the O-migration mechanism). Therefore, one may expect that HOR in Ni/YSZ may proceed via all three mechanisms, corresponding to the experimental result by Nagasawa et al.[58,59]

Most of the up-to-date DFT studies on hydrogen oxidation at the zirconia-based TPBs have been performed for YSZ, which allows us to quantitatively compare the present results for the Y-doped system with the literature data. However, the literature does not incorporate the OCV correction; therefore, a fair quantitative comparison between our energy barriers and the literature data should be performed using non-corrected values, which for the on-boundary mechanism are presented in Table 5. The barrier for the rate-limiting step 4-5 of the on-boundary mechanism (1.41 eV) is within the range of 0.41-1.43 eV reported for this step for various Y-doped TPB structures[3–5,7,13], with the lowest barrier reported by Cucinotta *et al.*[4] and the highest by Ammal *et al.*[5]. Transfer of the second hydrogen atom from the nickel surface to the hydroxyl at the interface (step 7-8) is associated with a barrier of 0.95 eV, which is comparable with the range of 0.80-1.23 eV reported for this step in the literature[4,5,7]. The OCV correction does not change the magnitude for the energy barrier of the rate-limiting step (1-2) of the O-migration mechanism; therefore, the barrier (1.26 eV) for this step at the Y-doped TPB can be directly compared with the literature data[3–5,7,13]. For instance, the value of 1.26 eV is exactly the same as the estimation obtained by Shishkin *et al.*[3].

Now let us continue results with the individual OCV correction for other dopants species. In the Sc- and Ce-doped systems, the H-migration mechanism should be favored; in the Sc-doped system, the activation barrier of the H-migration mechanism (1.02 eV) is the smallest among the other dopants. Moreover, dissociation of the water molecule dissociation observed at the Sc-based

TPB for the on-boundary mechanism, can contribute to the HOR via the H-migration mechanism. After dissociation of the water molecule, adsorbed OH does appear on top of dopant D_1. Now, let us consider that such an adsorbed OH is located near the two H atoms in state 11 of the H-migration mechanism. In this situation, according to Cucinotta *et al.*[4], the water molecule can be formed by the two H atoms and surface O with a much smaller endothermic effect than that with the identical process on a dry zirconia surface (no adsorbed OH). Thus, the dissociation of the water molecule observed at the Sc-doped TPB for the on-boundary mechanism can contribute to the H-migration mechanism with water molecule formation on the zirconia surface. This argument strengthens our conclusion that doping with Sc seems to be the most promising for promotion of the H-migration mechanism.

Ni/Scandia-stabilized zirconia (ScSZ) anode material has been experimentally reported to provide better SOFC performance than Ni/YSZ[33,60]. In particular, higher power density and lower anode overpotential were reported for Ni/ScSZ than for Ni/YSZ[33]. Our work partially supports better performance of Ni/ScSZ due to smaller activation barrier of the dominant HOR mechanism for Sc (1.02 eV, H-migration mechanism) than for Y (1.20 eV, on-boundary mechanism). However, besides the activation energy of HOR, dopants affect many other anode properties such as ionic conductivity, microstructure, etc. that are important for SOFC performance. Since our model does not include Sc dopants in the bulk region, and we do not consider the dopant effect on the oxide ion diffusion in bulk, different dominant HOR mechanisms found in our study for Ni/ScSZ and Ni/YSZ can be only a part of explanation for the experimentally observed higher activity of Ni/ScSZ in comparison with Ni/YSZ.

The O-migration mechanism should be the most favorable at the Al-doped TPB; the barrier for the rate-limiting step 1-2 is only 0.87 eV, which is significantly smaller than the activation energies for the other two mechanisms with Al. Moreover, compared with other dopants, Al provides the smallest activation energy of the O-migration mechanism. Thus, Al is the best candidate (among the examined species) to make the O-migration mechanism the most favorable HOR mechanism if Al can maintain the doped position during HOR.

As for Ca, the present results do not allow to make conclusive comment on the favorable reaction mechanism. HOR via the O-migration and on-boundary mechanisms cannot be completed due to the OH migration from the nickel surface back to zirconia and H_2O dissociation, respectively. As for the remaining H-migration mechanism, the barrier for Ca is the highest among all the dopants.

For co-doping to YSZ, the most favorable reaction mechanism for each of the Al, Sc, Ca co-dopants is the same as in the case of individual OCV correction. Only for the Ce co-dopant, the most favorable mechanism becomes the on-boundary mechanism (activation energies of on-boundary and H-migration mechanisms are actually same, but, as previously explained in this section, the on-boundary mechanism is regarded as dominant in this situation). As for the additionally considered co-dopants, the Mg co-dopant favors the O-migration mechanism with an activation barrier of 1.23 eV, while the Sr co-dopant favors the on-boundary mechanism with an activation energy of 1.54 eV.

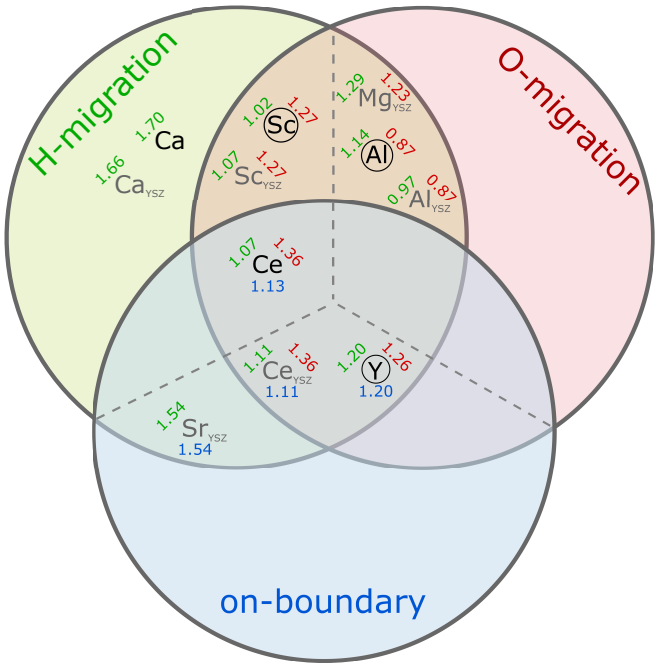

Fig. 8 Venn diagram illustrating those HOR mechanisms that can be successfully completed for each dopant species. The most favorable reaction mechanism (with energy barriers (eV)) for each dopant can be identified by the position of the dopant label in the corresponding sector depicted by the gray dashed lines.

We conclude the above discussion of this section with a Venn diagram (Fig. 8) where each dopant is located in the intersection area of the HOR mechanisms that can be successfully completed for that dopant. The most favorable reaction mechanism for each dopant can be identified by the position of the dopant in one of the three sectors formed by the gray dashed lines. The activation energies of the rate-limiting steps are provided near the label for each dopant. The color of the activation energy corresponds to the color of the reaction mechanism. A co-doping situation is marked with "YSZ" as a subscript. For each reaction mechanism, those dopants that favor the mechanism with the lowest activation energy after individual OCV correction are encircled.

Let us finally estimate the temperature effect. Our approach here is based on a simple adding entropic contribution of the gas molecules (H_2 and H_2O), and the temperature effect is discussed at a representative SOFC operating temperature of 1000 K. To obtain reaction energy profiles at 1000 K, the following three changes must be applied to the reaction energy profiles at 0 K:

- each $\frac{1}{2}H_2$ adsorption step has 0.68 eV higher reaction energy at 1000 K than that at 0 K,
- each H_2O desorption step has 1.96 eV lower reaction energy at 1000 K than that at 0 K,
- the OCV correction term U is 0.30 eV smaller at 1000 K than that at 0 K.

Similarly to Table 5 that is for 0 K, Table S1 (ESI†) summarizes activation energies and rate-limiting steps of all examined

reaction mechanisms for 1000 K. The rate-limiting step of each reaction mechanism remains the same at 1000 K as at 0 K. In addition, for all dopants except for Y, the dominant reaction mechanism is the same at 1000 K as at 0 K. Therefore, the only significant qualitative difference between the results for 0 and 1000 K is that the most favorable reaction mechanism at the Y-doped TPB changes at 1000 K to the O-migration from the on-boundary mechanism at 0 K. However, this estimation of the temperature effect is based on a simple adding the entropy contributions of the gas molecules. Considering the small difference (0.09 eV) between the activation energies of the on-boundary and O-migration mechanisms at 1000 K for the Y-doped TPB, we believe that to make an accurate estimation of the temperature effect one must perform vibrational analysis of the entire TPB system.

In the next section we present explanations for the low activation barrier of the O-migration mechanism at the Al-doped TPB and for the dissociation of the water molecule observed for some dopants at the TPB in the course of the on-boundary mechanism. The Al-doped TPB is used as an example. These findings may help to gain theoretical ideas on how to control the dominant mechanism of the HOR in an SOFC anode.

4.2 Details of HOR at Al-doped TPB

4.2.1 O transfer from TPB to nickel

The origin of the low activation barrier for the O-migration mechanism at the Al-doped TPB can be understood from an atomic coordination analysis of state 1. Figure 9 illustrates the TPB region of state 1 in a) Y- and b) Al -doped systems. For clarity, the simulation cell is partially repeated along the TPB line, so that the cation at site D_2 is depicted twice. Chemical bonds between cation X (X=Y, Al, Zr) and an oxygen ion are depicted when the distance between them is shorter than $1.2 \times (r_{\mathrm{X}}^{\mathrm{ion}} + r_{\mathrm{O}}^{\mathrm{ion}})$, where $r_{\mathrm{X}}^{\mathrm{ion}}$ and $r_{\mathrm{O}}^{\mathrm{ion}}$ are the ionic radii of cation X and the oxygen ion, respectively (see Table 6)[61]. According to the depicted bonds, the coordination number (CN) of both Y dopants is calculated as 7 in the Y-doped system; six oxygen ions bonded with the cations can be observed in Fig. 9a, and one more oxygen is positioned underneath each dopant, which is not shown in the figure. This coordination corresponds to the coordination at the ideal cut of the (111) surface of cubic zirconia, i.e., the Y-doped zirconia surface undergoes only a minor relaxation (Fig. 9a). In contrast, at the Al-doped TPB, the CNs of dopants at sites D_1 and D_2 are 4 and 5, respectively, and the zirconia surface is notably perturbed. Lower CNs of Al dopants can be recognized by the tendency of Al ions to have tetrahedral coordination due to sp^3 hybridization. Tetrahedral coordination can be clearly observed for Al dopant at the D_2 site (Fig. 9b), which is bonded with oxygen ions at sites a_1, a_2, b_2, and another oxygen ion underneath the dopant. The lengths of these four bonds are between 1.77 and 1.90 Å, and the angles between the bonds are within the range of $99.4 - 119.1^{\circ}$. The Al dopant at site D_1 cannot accomplish such perfect tetrahedral coordination, but shows a tendency for it by having CN=5. The length of these five bonds $d_{\mathrm{D_1-O}}$, is within the range of +1% to +7% from the $r_{\mathrm{Al}}^{\mathrm{ion}} + r_{\mathrm{O}}^{\mathrm{ion}}$ value (see Table 6). Lower CNs of Al dopants indicate that some surface oxygen ions have smaller CNs than normally coordinated (CN=3) surface oxygen atoms on the (111) surface. For example, in Fig. 9b, the surface oxygen ions at a_1 and b_1 sites are twofold coordinated because they are not connected with Al dopant at D_1 site. The distance between D_1 and b_1 sites $d_{\mathrm{D_1-b_1}}$, is 2.39 Å, which is 28% larger than the $r_{\mathrm{Al}}^{\mathrm{ion}} + r_{\mathrm{O}}^{\mathrm{ion}}$ value. The appearance of the twofold coordinated oxygen ions on the Al-doped ZrO_2 surface is in agreement with the work by Xu et al.[23].

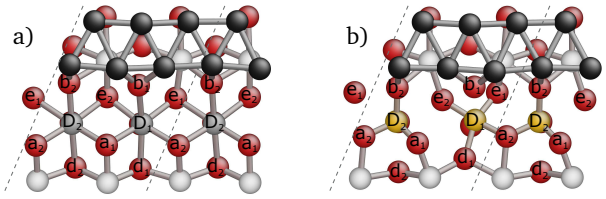

Fig. 9 Top view of a) Y- and b) Al-doped TPB regions in the reactant structure (state 1 of all reaction mechanisms). The structure is partly replicated along the TPB line; actual borders of the simulation cell are depicted by dashed gray lines. Only part of the bottom nickel layer and part of the top O-Zr-O trilayer are shown. Atoms are labeled and colored in the same way as Fig. 1 and 4. Y and Al dopants are shown in gray and yellow, respectively.

Considering that the $d_{\mathrm{D_1-b_1}}$ distance at the Al-doped TPB is 28% larger than $r_{\mathrm{Al}}^{\mathrm{ion}} + r_{\mathrm{O}}^{\mathrm{ion}}$, it can be expected that the twofold coordinated oxygen ion at the b_1 site is bonded more weakly to the zirconia surface than the surface oxygen ions with normal surface coordination. This is supported in Table 4; the migration of an oxygen ion from site b_1 (CN=2) to the nickel surface is associated with a lower endothermic effect (ΔE_{Omig}) of 0.78 eV than the migration of an oxygen ion from a b_2 site (CN=3). Thus, we consider that the twofold coordination of the oxygens ion at b_1 sites leads an energy barrier for the transfer of the ion to the nickel surface at the Al-doped TPB that is around 0.4 eV lower than that with the Y-doped system.

4.2.2 Dissociation of water molecule at TPB

To clarify the origin of water molecule dissociation at the Al- and Sc-doped TPBs during the on-boundary mechanism, we performed auxiliary relaxation of a structure with atomic positions taken from the relaxed Y-doped structure in state 8 of the on-boundary mechanism (with molecularly adsorbed water) with both Y dopants being replaced with either Al or Sc.

Let us first briefly inspect the relaxed Y-doped structure in state 8 of the on-boundary mechanism. Figure 10a depicts the atomic arrangement near the water molecule. The water molecule is located on top of the Y dopant at a D_1 site. The $D_1 - b_1$ distance, 2.47 Å, is slightly larger than 2.32 and 2.39 Å reported by Chaopradith *et al.* for a water molecule adsorbed on YSZ surface[55]. The $H_{H_2O} - O_{ZrO_2}$ distances are 2.77 and 3.37 Å, which suggests that there are no H-bonds between the hydrogens and surface oxygen ions.

Now let us proceed with the Al-doped structure. Figures 10a-d show the development of the atomic arrangement near the water molecule during relaxation of the Al-doped structure. The

Table 6 Ionic radius r_X^{ion} of cation X (X=Y, Al, and Zr)[61] with certain CN. The distance between the dopant at the D_1 site and the oxygen ion at the b_1 site, i.e., $d_{D_1-b_1}$, in state 1 is given with its deviation (in parenthesis) from the $r_X^{ion}+r_O^{ion}$. The last column, d_{D_1-O}, presents the range of bond lengths between dopants at site D_1 and oxygen ions that were accounted for the CN analysis

Ion	CN	r_X^{ion}, Å	$r_X^{ion}+r_O^{ion}$, Å	$d_{D_1-b_1}$, Å	d_{D_1-O}, Å
Y	7	1.10	2.34	2.32 (-1%)	2.24-2.41 (-5%-+3%)
Al	5	0.62	1.86	2.39 (+28%)	1.89-1.99 (+1%-+7%)
Zr	7	0.92	2.16		

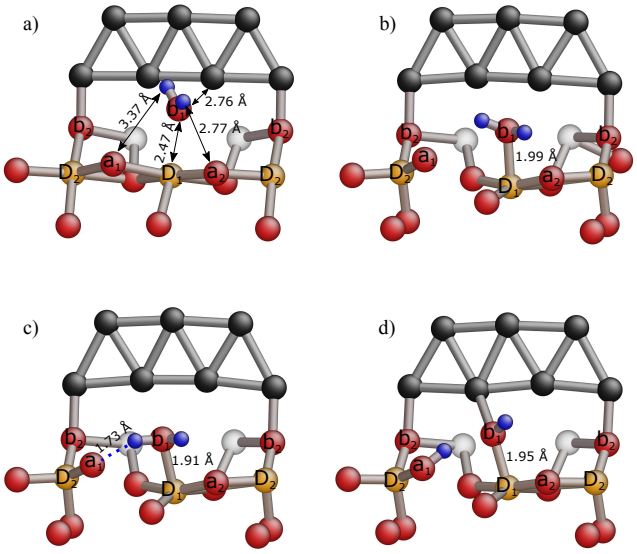

Fig. 10 Relaxation of Al-doped TPB with initially introduced water molecule on-top of the dopant at the D_1 site. a) Side view of the initial structure, where the atomic positions are identical to those in relaxed Y-doped TPB in state 8 of the on-boundary mechanism, b) structure after 80 relaxation steps and c) after 100 relaxation steps, d) and relaxed structure after 250 relaxation steps. Dopants at sites D_1 and D_2 are shown in yellow and hydrogen atoms are shown in blue.

relaxation begins with shortening of the distance between Al at a D_1 site and an oxygen ion at a b_1 site (see Fig. 10b), which can be explained by the smaller ionic radius of Al than Y. The relaxation proceeds with a decrease of the distance between one of the hydrogen atoms and one of the surface oxygen ions (Fig. 10c), which results in H-bond formation between one the hydrogen atoms and oxygen ion at an a_1 site. The transfer of the hydrogen then occurs from the water molecule to the surface oxygen ion, which results in the dissociation of the water molecule (Fig. 10d). Qualitatively similar results were obtained during relaxation of the structure doped with Sc.

It should be noted that the dissociative adsorption of water on a YSZ surface has been reported in a DFT calculation, and that dissociative adsorption was reported as much stronger than molecular adsorption[54,55]. In our present calculation, an artificial Y-doped structure with a dissociated water molecule was also confirmed as a more energetically stable configuration than state 8 of the Y-doped structure in the on-boundary mechanism (i.e., molecularly adsorbed water). To make the artificial structure, we manually built a Y-doped structure with a dissociated water molecule, where one hydroxyl was placed on top of dopant at a D_1 site and one hydrogen atom bonded to the surface oxygen ion at an a_1 site (this structure is qualitatively similar to the structure in Fig. 10d). The energy of the artificially made Y-doped structure is 0.4 eV lower than that of state 8. However, the barrier for such dissociation from state 8 was estimated to be 2.2 eV, which should be due to the large $H_{H_2O}-O_{ZrO_2}$ distances (2.77 and 3.37 Å) at the Y-doped TPB in state 8 (Fig. 10a).

The present study shows that the barrier-less dissociation of a water molecule occurs mainly when there are cations of small ionic radii (such as Al, Mg, Sc) at the TPB, which allows the water molecule to closely approach the zirconia surface and dissociate. Thus, to prevent water molecule dissociation and make water formation plausible via the on-boundary mechanism, it would be reasonable to choose a dopant with an ionic radii that is comparable or larger than that of Zr, so that the water molecule formed on top of the dopant at the TPB would not closely approach the zirconia surface.

5 Conclusions

DFT studies were performed with respect to the effect of cation dopants on the energy barriers of three different mechanisms for the HOR at the pore/nickel/zirconia TPB: on-boundary, O-migration, and H-migration mechanisms. OCV correction was applied to relate the present DFT results with the situation of anodic equilibrium in an SOFC. The results obtained can be summarized as follows:

1. At Y-doped TPBs, the HOR should proceed via the on-boundary mechanism when a water molecule is generated in close proximity to the TPB, which in a good agreement with the literature data. Co-doping of YSZ with Ce may increase the rate of the on-boundary mechanism.

2. Doping with Al shows potential to make the O-migration mechanism favorable. The low energy barrier for O transfer at Al-doped TPBs has been explained by the tetrahedral coordination of Al dopants and the appearance of twofold coordinated oxygen ions on the zirconia surface.

3. Sc could be the best dopant candidate to make the H-migration mechanism favorable (when used as either a major or a minor dopant).

4. Dopants with small ionic radii, such as Al, Mg, and Sc would hinder the on-boundary mechanism due to barrier-free water dissociation at the TPB. Co-doping by Mg should favor the O-migration mechanism.

5. Although dissociation of a water molecule, observed at the TPB for some dopants, hinders the on-boundary mechanism,

the dissociation of a water molecule can facilitate the HOR via the H-migration mechanism with water molecule formation on the zirconia surface.

6. Doping with Ca and Sr would hinder the O-migration mechanism due to the OH migration from the nickel surface back to zirconia. Doping and co-doping by Ca favor the H-migration mechanism. Co-doping by Sr should favor the on-boundary mechanism.

Conflicts of interest

There are no conflicts to declare.

Acknowledgements

This work was supported by the Japan Science and Technology Agency (JST)-CREST project for Phase Interface Science of Highly Efficient Energy Utilization (JPMJCR11C2, 11103789).

Notes and references

1 M. Shishkin and T. Ziegler, *J. Phys. Chem. C*, 2009, **113**, 21667–21678.
2 M. Vogler, A. Bieberle-Hütter, L. Gauckler, J. Warnatz and W. Bessler, *J. Electrochem. Soc.*, 2009, **156**, B663–B672.
3 M. Shishkin and T. Ziegler, *J. Phys. Chem. C*, 2010, **114**, 11209–11214.
4 C. S. Cucinotta, M. Bernasconi and M. Parrinello, *Phys. Rev. B*, 2011, **107**, 206103–1–206103–5.
5 S. C. Ammal and A. Heyden, *J. Phys. Chem. Lett.*, 2012, **3**, 2767–2772.
6 M. Shishkin and T. Ziegler, *Phys. Chem. Chem. Phys.*, 2014, **16**, 1798–1808.
7 S. Liu, T. Ishimoto, D. S. Monder and M. Koyama, *J. Phys. Chem. C*, 2015, **119**, 27603–27608.
8 D. G. Goodwin, H. Zhu, A. M. Colclasureand and R. Kee, *J. Electrochem. Soc.*, 2009, **156**, B1004–B1021.
9 W. G. Bessler, M. Vogler, H. Störmer, D. Gerthsen, A. Utz, A. Weber and E. Ivers-Tiffee, *Phys. Chem. Chem. Phys.*, 2010, **12**, 13888–13903.
10 H. Kohno, S. Liu, T. Ogura, T. Ishimoto, D. S. Monder, K. Karan and M. Koyama, *ECS Transactions,*, 2013, **57**, 2821–2830.
11 A. Bieberle, L. Meier and L. Gauckler, *J. Electrochem. Soc.*, 2001, **148**, A646–A656.
12 K. V. Hansen, K. Norman and M. Morgensen, *J. Electrochem. Soc.*, 2004, **151**, A1436–A1444.
13 Z. Fu, M. Wang, P. Zuo, Z. Yang and R. Wu, *Phys. Chem. Chem. Phys.*, 2014, **16**, 8536–8540.
14 R. Pornprasertsuk, P. Ramanarayanan, C. B. Musgrave and F. B. Prinz, *J. Appl. Phys.*, 2005, **98**, 103513–1–103513–7.
15 J. J. Plata, A. M. Márquez and J. F. Sanz, *Chem. Mater.*, 2014, **26**, 3385–3390.
16 S. Grieshammer, B. Grope, J. Koettgen and M. Martin, *Phys. Chem. Chem. Phys.*, 2014, **16**, 9974–9986.
17 J. Chevalier, L. Gremillard, A. V. Virkar and D. R. Clarke, *J. Am. Ceram. Soc.*, 2009, **92**, 1901–1920.
18 J. Kondoh, T. Kawashima, S. Kikuchi, Y. Tomii and Y. Ito, *J. Electrochem. Soc.*, 1998, **145**, 1527–1536.
19 H. Okazaki, H. Suzuki and K. Ihata, *Journal of the Physical Society of Japan*, 1994, **63**, 3556–3559.
20 H. Okazaki, H. Suzuki and K. Ihata, *Physics Letters A*, 1994, **188**, 291–295.
21 E. Lee, F. B. Prinz and W. Cai, *Phys. Rev. B*, 2011, **83**, 052301–1–052301–4.
22 M. C. Muñoz, S. Gallego, J. I. Beltrán and J. Cerdá, *Surf. Sci. Rep.*, 2006, **61**, 303–344.
23 J. Xu, Y. Higuchi, N. Ozawa and M. Kubo, *ECS Trans.*, 2015, **68**, 3187–3193.
24 A. M. Iskandarov, Y. Ding and Y. Umeno, *J. Phys.: Condens. Matter*, 2017, **29**, 045001–1–045001–12.
25 E. Muccillo and M. Kleitz, *J. Eur. Ceram. Soc.*, 1996, **16**, 453–465.
26 R. Muccillo, R. B. Netto and E. Muccillo, *Mater. Lett.*, 2001, **49**, 197–201.
27 H. Jung, K.-S. Hong, H.-G. Jung, H. Kim, H.-R. Kim, J.-W. Son, H.-W. Lee and J.-H. Lee, *J. Electrochem. Soc.*, 2007, **154**, B480–B485.
28 R. Knibbe, J. Drennan, A. Dicks and J. Love, *Int. J. Appl. Ceram. Technol.*, 2008, **179**, 511–519.
29 F. Wang, W. Wang, R. Ran, M. O. Tade and Z. Shao, *J. Power Sources*, 2014, **268**, 787–793.
30 F. Yu, J. Xiao, L. Lei, W. Cai, Y. Zhang, J. Liu and M. Liu, *Solid State Ionics*, 2016, **289**, 28–34.
31 X. Song, X. Dong, M. Li and H. Wang, *Solid State Ionics*, 2016, **308**, 58–64.
32 H. Orui, R. Chiba, K. Nozawa, H. Arai and R. Kanno, *Int. J. Appl. Ceram. Technol.*, 2013, **238**, 74–80.
33 H. Sumi, K. Ukai, Y. Mizutani, H. Mori, C.-J. Wen, H. Takahashi and O. Yamamoto, *Solid State Ionics*, 2004, **174**, 151–156.
34 T. Tada, *ECS Trans.*, 2015, **68**, 2875–2885.
35 T. Tada and S. Watanabe, *J. Phys. Chem. C*, 2009, **113**, 17780–17786.
36 C. L. Liu, J. M. Cohen, J. B. Adams and A. F. Voter, *Surface Science*, 1991, **253**, 334–344.
37 G. Ballabio, M. Bernasconi, F. Pietrucci and S. Serra, *Phys. Rev. B.*, 2004, **70**, 075417–1–075417–6.
38 X. Xia, R. Oldman and R. Catlow, *Chem. Mater.*, 2009, **21**, 3576–3585.
39 X. Xia, R. Oldman and R. Catlow, *J. Mater. Chem.*, 2011, **21**, 14549–14558.
40 W. Emam, A. F.Mabied, H. Hashem, M. Selim, A. El-Shabiny and I. A. Farag, *J. Solid State Chem.*, 2015, **228**, 153–159.
41 P. Satardekar and V. Sglavo, *Int. J. Appl. Ceram. Technol.*, 2015, **12**, E61–E67.
42 G. Kresse and J. Hafner, *Phys. Rev. B.*, 1993, **47**, 558–561.
43 G. Kresse and J. Furthmüller, *Phys. Rev. B.*, 1996, **54**, 11169–11186.
44 P. Blöchl, *Phys. Rev. B*, 1994, **50**, 17953–17979.

45 J. P. Perdew, K. Burke and M. Ernzerhof, *Phys. Rev. Lett.*, 1997, **77**, 3865–3868.
46 X. Xia, *Ph.D. thesis*, University College London, 2010.
47 S. L. Dudarev, G. A. Botton, S. Y. Savrasov, C. J. Hamphreys and A. P. Sutton, *Phys. Rev. B*, 1998, **57**, 1505–1509.
48 M. Nolan, S. Grigoleit, D. C. Sayle, S. C. Parker and G. W. Watson, *Surface Science*, 2005, **576**, 217–229.
49 G. Henkelman and H. Jónsson, *J. Chem. Phys.*, 2000, **113**, 9901–9904.
50 S. M. Foiles, M. I. Baskes, C. F. Melius and M. S. Daw, *Journal of the Less-Common Metals*, 1987, **130**, 465–473.
51 G. Kresse, *Phys. Rev. B*, 2000, **62**, 8295–8305.
52 J. Nørskov, J. Rossmeisl, A. Logadotirr, L. Lindqvist, J. Kitchin, T. Bligaard and H. Jóhnson, *J. Phys. Chem. B*, 2004, **108**, 17886–17892.
53 A. M. Iskandarov, A. Kubo and Y. Umeno, *J. Phys.: Condens. Matter*, 2015, **25**, 015005–1–015005–9.
54 M. Shishkin and T. Ziegler, *J. Phys. Chem. C*, 2008, **112**, 19662–19669.
55 D. Chaopradith, D. Scanlon and C. R. A. Catlow, *J. Phys. Chem. C*, 2015, **119**, 22526–22533.
56 M. Ihara, T. Kusano and C. Yokoyama, *J. Electrochem. Soc.*, 2001, **148**, A209–A219.
57 S. Primdahl and M. Mogensen, *J. Electrochem. Soc.*, 1997, **144**, 3409–3419.
58 T. Nagasawa and K. Hanamura, *ECS Trans.*, 2014, **64**, 117–134.
59 T. Nagasawa and K. Hanamura, *ECS Trans.*, 2015, **68**, 1315–1322.
60 K. Nomura, Y. Mizutani, M. Kawai, Y. Nakamura, O. Yamamoto and O. Yamamoto, *Solid State Ionics*, 2000, **132**, 235–239.
61 J. E. Huheey, E. A. Keiter and R. L. Keiter, *Inorganic chemistry: principles of structure and reactivity, 4th Ed.*, Harper-Collins Colledge Publishers, New York, USA, 1993.

The H_2 oxidation mechanism at the pore/nickel/zirconia triple phase boundary is drastically changed depending on dopants at the boundary.

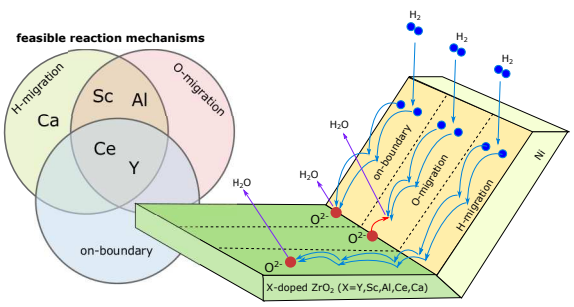
feasible reaction mechanisms
H-migration
O-migration
Sc
Al
Ca
Ce
Y
on-boundary
H2O
H2O
H2O
H2
H2
H2
O2-
O2-
O2-
on-boundary
O-migration
H-migration
Ni
X-doped ZrO2 (X=Y,Sc,Al,Ce,Ca)